CHEMICAL IMAGING

Raman microscopy of cryofixed biological specimens for high-resolution and high-sensitivity chemical imaging

Kenta Mizushima[1,2], Yasuaki Kumamoto[1,3], Shoko Tamura[4], Masahito Yamanaka[1], Kentaro Mochizuki[4], Menglu Li[1,2], Syusuke Egoshi[5,6], Kosuke Dodo[5,6], Yoshinori Harada[4], Nicholas I. Smith[7], Mikiko Sodeoka[5,6], Hideo Tanaka[4,8], Katsumasa Fujita[1,2,3]*

Raman microscopy is an emerging molecular imaging technology, yet its signal-to-noise ratio (SNR) in measurements of biological specimens is severely limited because of the small cross section of Raman scattering. Here, we present Raman imaging techniques of cryofixed specimens to overcome SNR limitations by enabling long exposure of specimens under highly stabilized low-temperature conditions. The observation of frozen specimens in a cryostat at a constant low temperature immediately after rapid freezing enabled the improvement of SNR and enhanced the spatial and spectral resolution. We also confirmed that the cryofixation can preserve physicochemical states of specimens by observing alkyne-labeled coenzyme Q in cytosol and hemeproteins in acute ischemic myocardium, which cannot be done by fixation using chemical reagents. Last, we applied the technique for multiplex Raman imaging of label-free endogenous molecules and alkyne-tagged molecules in cryofixed HeLa cells, demonstrating its capability of high-content imaging of complex biological phenomena while maintaining physiological conditions.

INTRODUCTION

Raman microscopy is an emerging tool for molecular analysis of biological specimens under physiological conditions (*1*, *2*). Distributions of biomolecules in a sample are imaged by obtaining the spatial distributions of Raman scattering, allowing the visualization of cell dynamics (*3*), drug effects (*4*–*6*), and cell differentiations (*7*, *8*). Interpreting sample-specific Raman spectra and their spatial distributions, Raman microscopy enables label-free and nondestructive classification of cells and tissues (*9*–*11*), which recently is a leading interest in the fields of biomedicine and regenerative medicine (*12*, *13*). The use of Raman tags has further extended Raman microscopy as a technique to track exogenous or endogenous small molecules (*14*, *15*). This strategy has enabled super multiplex imaging that exploits the narrow line emission of Raman probes for simultaneous visualization of a large number of targets (*16*, *17*).

One of the challenges in Raman microscopy is to improve the signal-to-noise ratio (SNR) in hyperspectral imaging. The intrinsic small cross section of Raman scattering has limited the detection sensitivity and the resolutions in the spatial and spectral domains. High-intensity laser irradiation may increase the number of Raman scattering photons but can easily degrade the specimen. Using low-intensity laser irradiation can prevent alterations of biological specimens but then requires a long acquisition time in Raman imaging, leading to motion artifacts as well as physiological changes of specimens during observation. To overcome these problems, the spatial resolution and field of view (FOV) are sacrificed in a trade-off with image acquisition time (*18*–*20*). The sample fixation by chemical reagents [e.g., paraformaldehyde (PFA)] or organic solvents has been used for suppressing the motion of biological specimen and preserving biomolecules (*21*, *22*) but denatures cells by chemical reaction or dehydration (*20*, *21*, *23*). In addition, the utility of the chemical fixation is limited in fixing biological activities in motion (*24*), and there are molecular species that cannot be fixed by the current chemical fixation techniques (*25*).

Here, we present a technique for high-SNR Raman imaging of biological specimens while preserving their physicochemical states under a low temperature. Cryopreservation of biological specimen was achieved by rapid freezing with liquid cryogen and subsequent cooling for low-temperature Raman observation. Long-term Raman imaging of the frozen specimen was enabled by a customized microscope cryostat that can maintain the specimen under low temperature. We confirmed the improvement of SNR with a longtime exposure without causing obvious sample photodegradation. The wide FOV and high-resolution measurement was also realized while avoiding motion blur in Raman imaging. We also confirmed that the redox state of hemeproteins in a heart tissue, which changes rapidly at physiological temperature (~310 K), was preserved by cryofixation and visualized by low-temperature Raman imaging, demonstrating the capability of preserving chemical states of proteins. Low-temperature Raman imaging was performed to understand protein crystallization (*26*) and the condition of intra- and extracellular molecules under cryopreservation of biological samples (*27*). This approach is also beneficial to improve the sensitivity and the spatial and spectral resolution in Raman imaging. The technique presented in this research enables high-resolution and high-sensitivity chemical imaging of biological specimens after rapid freezing and expands the advantage of cryogenic Raman measurement further.

[1]Department of Applied Physics, Osaka University, Suita, Osaka 565-0871, Japan. [2]Advanced Photonics and Biosensing Open Innovation Laboratory, AIST-Osaka University, AIST, Suita, Osaka 565-0871, Japan. [3]Institute for Open and Transdisciplinary Research Initiatives, Osaka University, Suita, Osaka 565-0871, Japan. [4]Department of Pathology and Cell Regulation, Kyoto Prefectural University of Medicine, Kamigyo-ku, Kyoto 602-8566, Japan. [5]Synthetic Organic Chemistry Laboratory, RIKEN Cluster for Pioneering Research, Wako, Saitama 351-0198, Japan. [6]Catalysis and Integrated Research Group, RIKEN Center for Sustainable Resource Science, Wako, Saitama 351-0198, Japan. [7]Biophotonics Laboratory, Immunology Frontier Research Center, Osaka University, Suita, Osaka 565-0871, Japan. [8]Faculty of Health and Medical Science, Kyoto University of Advanced Science, Ukyo-ku, Kyoto 615-8577, Japan.
*Corresponding author. Email: fujita@ap.eng.osaka-u.ac.jp

RESULTS

An inverted Raman microscope equipped with a custom cryostat that enables rapid freezing and low-temperature observation was developed (Fig. 1, A and B). A specimen on a fused silica coverslip was placed on the sample mount in the cryostat, separated from the cooling block by a 20-μm-height stainless spacer that prevents cell damage that would, otherwise, occur by its direct contact to the cooling block. The cooling block was equipped with a thermocouple, a liquid nitrogen circulation channel, and a heater for temperature control of the sample. Flow of nitrogen gas in the cryostat prevents frost generation that could occur around the sample during the cooling and observation processes.

The sample was cryofixed by rapid freezing using liquid propane at 88 K (in an amount of 40 to 60 ml) to avoid destruction of cell structures by large ice crystal formation (*28*–*30*). Immediately after applying the cryogen to the sample, circulation of liquid nitrogen in the cooling block was started to stabilize the temperature of the cooling block for Raman measurement. The liquid propane remaining on the sample, which could interfere with Raman measurement, was removed via evaporation or introducing liquid nitrogen on the sample (see Materials and Methods). The cryostat was sealed using a sapphire glass window and a rubber ring before Raman observation. We confirmed that there was no image blurring by observation of 0.2 μm beads (fig. S1) that could be potentially caused by vibration from the liquid nitrogen circulation after stabilization of the cooling block temperature.

We investigated local heating by laser irradiation in Raman observation of biological samples by simulation and experiment as shown in fig. S2. Flavin adenine dinucleotide (FAD) and reduced cytochrome c were assumed as main absorbers, their absorbance and intracellular concentration were measured to be used for the simulation by COMSOL (fig. S2, A to D). The temperature heating was calculated to be around 1 to 2 K after 70-s laser irradiation with the line illumination used in our experiment (fig. S2, E and F). Our simulation also shows that the temperature increase reaches the steady state in about 5 s under the laser intensity used in our measurement at around 234.3 K with an initial sample temperature of 233 K. The detailed parameters for the calculation are listed in table S1. We also experimentally confirmed that the local heating was not substantial by measuring the temperature-dependent O—H stretching band at around 3130 cm^{-1}, which can be used for monitoring sample temperature (*31*). In our experiment, the Raman band of O—H stretching mode in a HeLa cell was almost identical under the irradiation times of 5 and 40 s per line at 233 K (fig. S2, G and H), and its peak position was almost identical to that of pure water at 233 K. These experimental results confirm that there was no notable temperature increase during the low-temperature measurements that we performed.

We compared live-cell Raman images and spectra acquired under low temperature (233 K) and room temperature (293 K). The Raman images reconstructed at 750 cm^{-1} (porphyrin breathing of cytochromes), 1680 cm^{-1} (amide I of proteins), and 2850 cm^{-1} (symmetric CH_2 stretching of lipids) of cryofixed cells also show the contrasts similar to those of living cells (Fig. 1C). Although an ice crystal peak was shown in the Raman spectra at the observation area (fig. S3A), we did not observe destruction of cell body and intracellular organelles in a Raman image of cryofixed cells (fig. S3B). The growth of large crystal could have been suppressed by rapid freezing, since slow freezing at a rate of 1 K/min showed obvious destruction of sample structures (fig. S3C). These results indicate that the ice crystals that could form during rapid freezing and subsequent temperature rise to 233 K were small enough to make morphological perturbation of the samples negligible in optical observations.

Although many cellular Raman bands appeared similarly at the low and room temperatures, the Raman peaks at 1061 and 2880 cm^{-1}, which can be assigned to C—C stretching and asymmetric CH_2 vibrational modes of lipid, respectively (*32*), exhibited differences between cryofixed cells and living cells (Fig. 1D). The Raman images reconstructed from these bands (fig. S4A) show spatial distributions similar to that of lipid reconstructed from 2850 cm^{-1} (Fig. 1C). The increases in Raman signals at 1061 and 2880 cm^{-1} can be attributed to lipid-phase changes occurring at low temperature (233 K), at which the acyl chain of lipid is more ordered than at 293 K (*32*).

We also found that the resonant Raman scattering of intracellular molecules appeared differently at low temperatures. The Raman bands at 1153 and 1517 cm^{-1}, which can be assigned to the resonant Raman scattering of carotenoids (*33*), appeared only at the low-temperature measurements (Fig. 1D) and showed the spatial distributions resembling those of lipid droplets (fig. S4B) that can store hydrophobic vitamins (*34*). The bands at 917, 968, and 1337 cm^{-1} can be assigned to cytochromes (*35*, *36*), and their spatial distributions were similar to cytochromes reconstructed from 750 cm^{-1} (fig. S4C). The band at 1298 cm^{-1} can also be assigned to cytochromes (*35*), while it can be assigned also to twisting deformational CH mode of lipid (*32*). The spatial distribution of the 1298 cm^{-1} band was similar to mixture of those of cytochromes and lipid (fig. S4D). The photobleaching effects in resonant Raman scattering from cytochromes and carotenoids (*36*–*38*) could be suppressed and appeared in the low-temperature measurement. To further investigate the temperature dependence of Raman spectra of biological molecules, we compared the Raman spectra of bovine serum albumin, phenylalanine, and 5-ethynyl-2′-deoxyuridine (EdU), a commonly used Raman tag as a benchmark, between room and low temperatures. Notable change in Raman spectra that prevents identification of intracellular molecules was not recognized, even with the change of baseline due to the change in water spectrum, which is typically removed by baseline correction (fig. S5).

The high stability of sample condition is beneficial to improve the spectral and spatial resolution in Raman imaging, allowing the accumulation of Raman photons. In principle, the spectral resolution can be improved by using a spectrophotometer with higher wavelength dispersion and a narrower entrance slit, which are not always applicable because the Raman signal decreases under these conditions, especially in live-cell Raman imaging, where the SNR is typically restricted because of the limitation of exposure time to avoid the sample photodamage (Fig. 1E). This limitation is markedly mitigated in low-temperature Raman imaging, and both high spectral and spatial resolutions can be achieved by long exposure with compensating the loss of Raman photons (Fig. 1, E and F). The bandwidth of phenyl ring breathing mode of phenylalanine at 1001 cm^{-1} was 4.4 cm^{-1} for the low-temperature measurement with higher wavelength dispersion and a narrower entrance slit and 7.3 cm^{-1} for the live-cell Raman measurement at room temperature with lower wavelength dispersion and a wider entrance slit (Fig. 1F). Because the estimated phenylalanine bandwidth does not show clear temperature dependence at this temperature range (fig. S6), the improvement of spectral resolution was fully attributed to the wavelength dispersion and the entrance slit width.

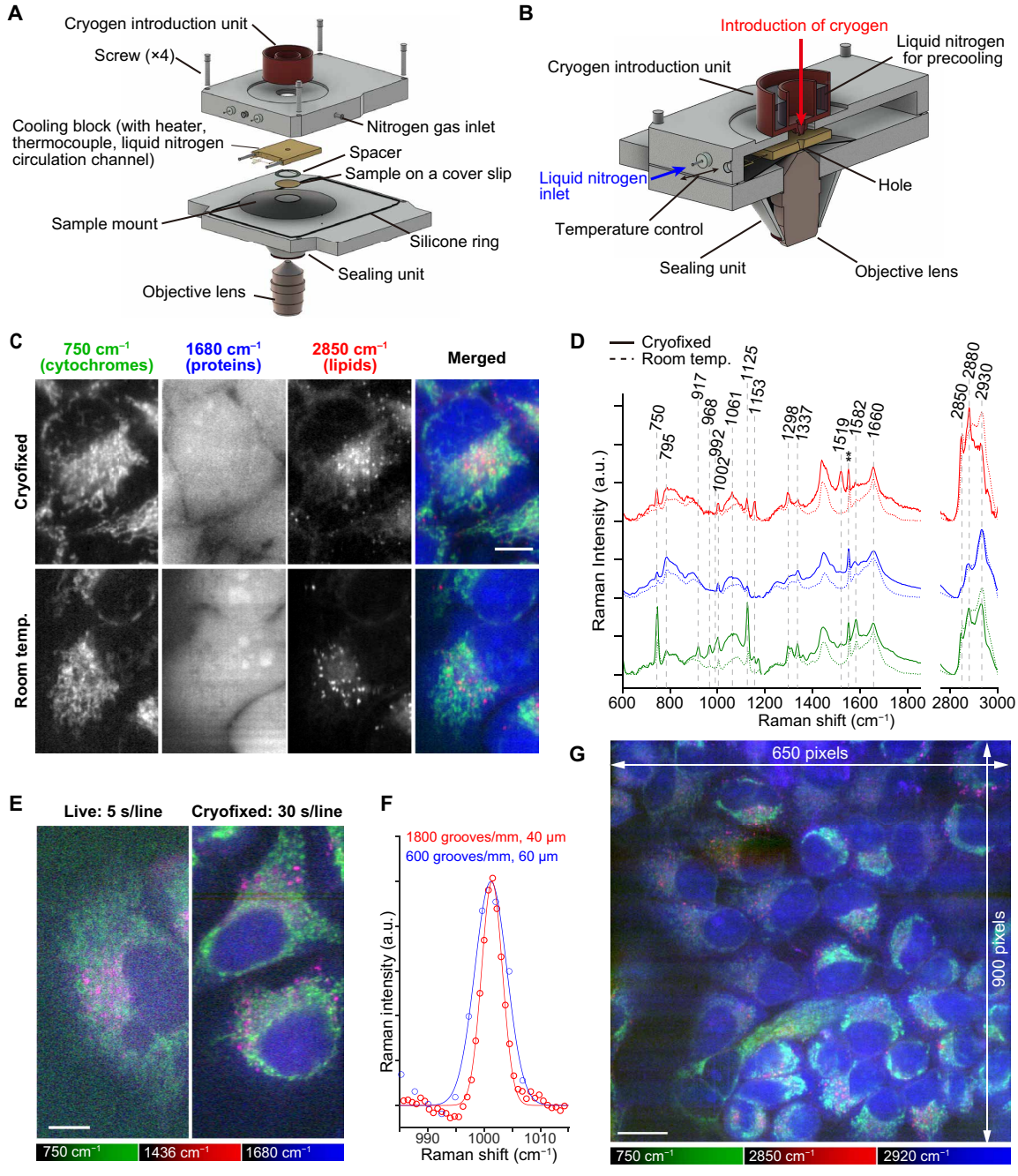

Fig. 1. Raman imaging of cryofixed HeLa cells frozen rapidly and measured at a low temperature, enabled by development of a custom cryostat equipped with a cryogen introduction unit. (**A**) The components of the cryostat equipped with a cryogen introduction unit, together with the sample and objective lens. (**B**) The assembled cryostat. (**C**) Raman images of the rapidly frozen HeLa cells and live HeLa cells. (**D**) Raman spectra of the rapidly frozen HeLa cells, acquired with the custom cryostat (at 233 K, solid lines). Room temperature (293 K) results are shown with dashed lines for comparison. In the spectra, atmospheric oxygen band was seen (~1550 cm^{-1}) (**). The red, blue, and green lines show spectra taken from the regions rich in lipids, nucleus, and cytoplasm, respectively. Spectra with different colors were vertically offset. (**E**) Raman images acquired with a high–spectral resolution setting. The live and cryofixed images were acquired at 293 and 233 K, respectively. Exposure times were 5 and 30 s per line for imaging the live and cryofixed samples, respectively. (**F**) The Raman bands at 1001 cm^{-1} assigned to phenyl ring breathing of phenylalanine in HeLa cells, acquired at a high spectral resolution and cryofixed condition (red) and a low spectral resolution and room temperature (blue). Red and blue solid lines are fitted using Gaussian functions (a.u., arbitrary unit). (**G**) A wide-FOV Raman image of the cryofixed HeLa cells kept at 173 K. Exposure times: 5 s per line for (C) and 40 s per line for (G). Scale bars, 10 µm [(C) and (E)] and 20 µm for (G). Singular value decomposition (SVD) was applied to all data for noise reduction (*70*).

By maintaining the low temperature of the cooling block, we can maintain the chemical conditions of the sample and the spatial distributions of biomolecules. Taking advantage of this, we demonstrated high-resolution Raman imaging (650 × 900 image pixels) without obvious motion blur and sample drift for 10 hours (Fig. 1G). We kept the temperature of the cooling block at 173 K during measurement to avoid growth of large ice crystals in the frozen sample because recrystallization can occur more prominently at higher temperature (*39*).

The physical fixation by rapid freezing has several advantages in comparison to chemical fixation using organic chemical reagents. As shown in fig. S7, the cells fixed with PFA exhibited apparent photodamage by longtime laser exposure for high-SNR Raman imaging, possibly due to laser-induced heating (*40*) or generation of reactive oxygen species (*41*). On the other hand, at the low temperature, no notable alteration in molecular distributions of the sample was confirmed after the repetitive Raman imaging (Fig. 2A). We also confirmed that the Raman signal linearly increased along the exposure time (Fig. 2B), which indicates that the biological molecules were not degraded by high-dose laser irradiation and can improve the sensitivity for detecting molecules at low concentrations. We also confirmed the improvement of SNR in Raman measurement by extending exposure time (fig. S8A), although we observed the increase of autofluorescence and the O—H stretching modes that overlap C—H stretching modes at low temperature (fig. S9). It should be noted the rise of lipid Raman bands and resonant Raman bands at low temperature is beneficial to improve the SNR. In addition, increase of spectral background intensity with exposure time is less than linear due to photobleaching or transition to the dark state, whereas Raman signal increases linearly (fig. S8, B to D). We also measured EdU, an alkyne-tagged cell proliferation probe, which can be incorporated into cell nuclei, and confirmed that the distribution of EdU in cell nuclei was more clearly visualized with the longer exposure (Fig. 2C).

Another advantage of cryofixation by rapid freezing can include instant preservation of physicochemical state of intracellular molecules under living conditions. We confirmed this advantage by observing cytochromes and alkyne-tagged coenzyme Q (AltQ2), a mobile small molecule (*14*), using the developed system. The Raman signals of cytochromes and AltQ2 (Fig. 2D) decreased in the PFA-fixed cells due to oxidation of cytochromes (*20*) and spatial alteration of AltQ2 (*42*), whereas the cryofixed cells showed the distributions of cytochromes and AltQ2 similar to those in living cells (Fig. 2D). The result demonstrates that rapid freezing and subsequent low-temperature Raman imaging can preserve and observe various cellular components at an environment close to physiological conditions, which cannot be done using conventional chemical fixation techniques.

Taking the advantages of the presented technique, we performed a high-SNR and multicolor Raman imaging of cultured cells (Fig. 2E). In addition to Raman images of cytochromes, DNA/RNA (*43*), carotenoids, lipids, and proteins that are observed without labeling, three Raman tags—EdU, MitoBADY (*44*), and AltQ2—were simultaneously observed. We also obtained a Raman image of intracellular and extracellular water distributions, using the Raman signal that indicates ice crystal in and out of cryopreserved cells, which can be useful for understandings the conditions of cryopreserved cells (*45*). These results demonstrate the potential of cryo-Raman microscopy to detect the chemical response of endogenous molecules from their Raman spectra while using various Raman tags and probes (*14*, *17*, *46*) to perform highly multiplex observations.

A benefit of rapid freezing also lies in its ability to preserve transient biochemical reactions in biological specimens. One example is the redox state changes of cytochromes in myocardial ischemia (*47*). Previous Raman imaging techniques were able to reveal the redox state change but could not visualize the spatial distribution of the redox state in the heart at a specific time point. In this research, we conducted rapid freezing and low-temperature Raman imaging of rat myocardial tissues under ischemic and nonischemic circumstances.

We used low-temperature Raman imaging to enable redox imaging of an acute ischemic heart. Custom methodology and system were adapted for the experiment using heart tissues as follows. In this procedure, we first froze the right ventricle of myocardial tissue by liquid propane (Fig. 3A). After substituting the liquid propane with liquid nitrogen, the frozen tissue was moved into a microscope cryostat for an upright microscope (Fig. 3B). To prevent frost formation on the sample by humid air, we immediately sealed the cryostat with the microscope objective lens and rubber sheet.

Figure 3C shows the results of Raman hyperspectral imaging of rat hearts rapidly frozen at 1 and 21 min after cessation of Langendorff perfusion with oxygenated Tyrode's solution. Raman images reconstructed at 600 cm^{-1} show the distribution of reduced cytochrome c in cardiomyocytes. The signal intensity of reduced cytochrome c within the cardiomyocytes is greater in the heart after 21 min of ischemia compared to that after 1 min, which is consistent with the findings from single-point time-lapse Raman spectroscopy (*47*). The Raman spectra also reflect the trends seen in the Raman images of reduced cytochrome c (Fig. 3D). Other Raman bands assigned for reduced cytochrome c, including 750 and 1128 cm^{-1} were higher in the ischemic heart than in the nonischemic heart. In addition, the Raman band at 1640 cm^{-1}, identified as oxygenated myoglobin (*48*), showed an inverse trend to the reduced cytochrome c signal. Similar trends were confirmed by Raman spectroscopic measurements in live ischemic and nonischemic rat heat tissue (*49*). Our results suggest that the redox state of cytochrome c in cardiomyocytes was preserved by rapid freezing. In addition, we were able to acquire not only Raman spectra but also Raman images while preserving biochemical reactions by using cryofixation. The Raman image acquisition process took 27 min, during which an acutely ischemic heart would undergo changes in redox state and shape without cryofixation.

DISCUSSION

The combination of cryofixation and subsequent low-temperature measurement of biological specimens has overcome several limitations in Raman microscopy, realizing a high SNR and a large FOV as well as high spatial and spectral resolution. The technique substantially reduces photodamage and motion artifacts, allowing the visualization of intracellular molecules and subcellular structures invisible in the measurement without freezing while also enhancing quantification capabilities of Raman imaging (*50*–*51*). The cryofixation of chemical states, such as redox states, can further extend the advantage of Raman imaging in its capability of sensing molecular states and their environments. The low-temperature measurement combined with rapid freezing is also beneficial in coherent Raman microscopy, providing more precise morphological information and reducing the sample degradation by intense pulsed laser irradiation.

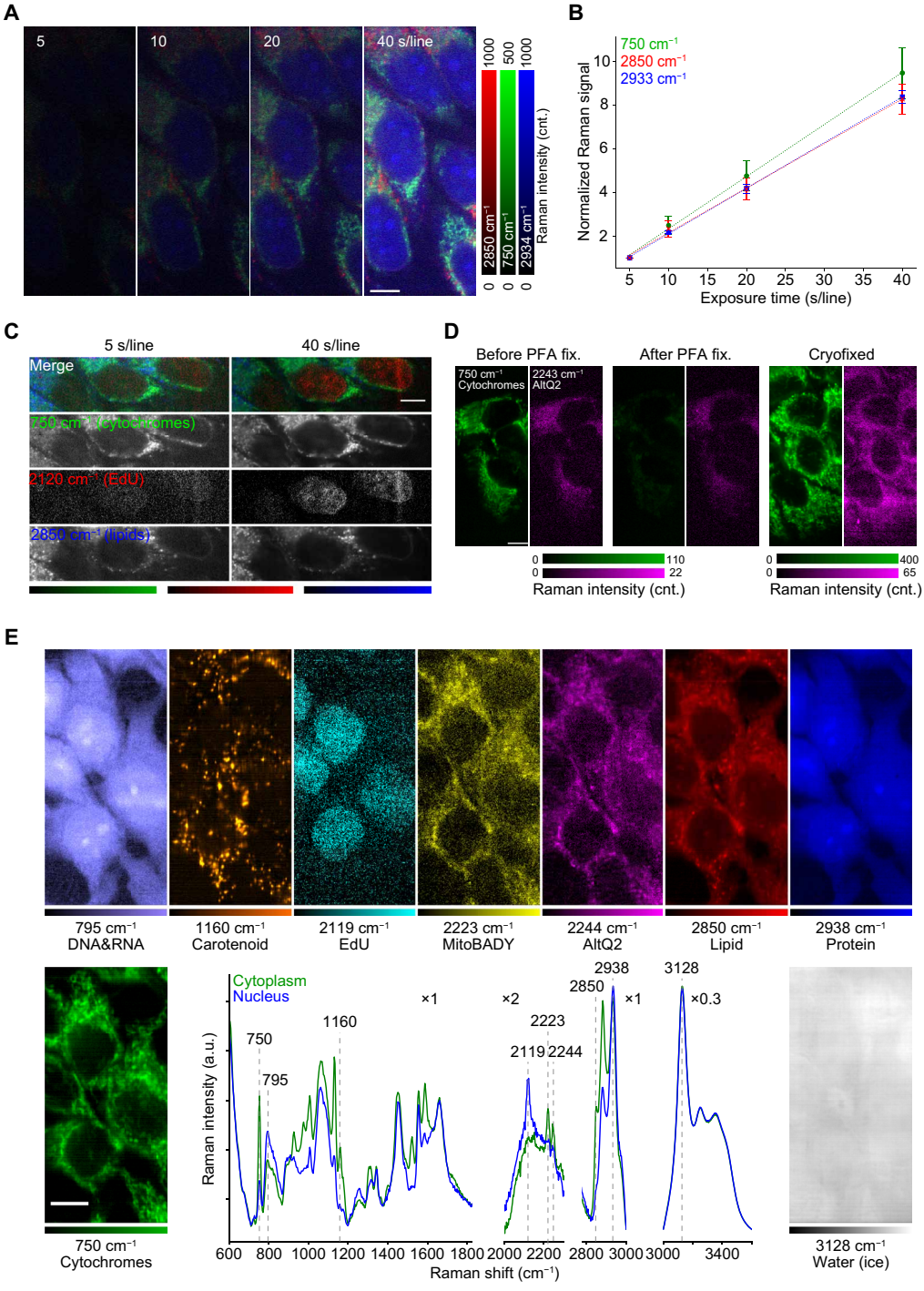

Fig. 2. High-SNR Raman imaging of HeLa cells with cryopreservation of physicochemical states. (**A**) Raman images of cryofixed HeLa cells acquired with exposure times of 5, 10, 20, and 40 s per line at 233 K. In data processing, no noise reduction was applied. (**B**) Raman signal at 750, 2850, and 2933 cm^{-1} of cryofixed HeLa cells to exposure time. The signal at each exposure time was normalized by the signal at 5 s per line for each Raman band. The normalized signals were averaged over 12 different regions in (A). Error bars show the standard deviation for each Raman band ($n = 12$). The dotted lines indicate fitting curves calculated by linear functions. In data processing, no noise reduction was applied. (**C**) Raman images representing EdU incorporated in cryofixed HeLa cells, acquired with exposure times of 5 and 40 s per line at 233 K. Cytochromes and lipids are also shown to clarify the localization of EdU in nuclei. (**D**) Raman images of living cells (left), chemically fixed cells (middle), and cryofixed cells (right). Measurement temperature were 293 K (left, middle) and 233 K (right). The images represent cytochromes (green) and AltQ2 incorporated in the cells (magenta). (**E**) Nine-color Raman images and spectra measured at 203 K for the cryofixed HeLa cells loaded with EdU, MitoBADY, and AltQ2. The green and blue lines were acquired from cytoplasm and nucleus, respectively. In the Raman spectra, the scales of lateral axes were modified in each wave-number region, respectively. Exposure time: 10 s per line for living cells and PFA-fixed cells in (D), 30 s per line for cryofixed cells in (D), and 70 s per line for (E). Scale bars, 10 μm. SVD was applied to data shown in (C) to (E) for noise reduction (*70*). cnt., counts.

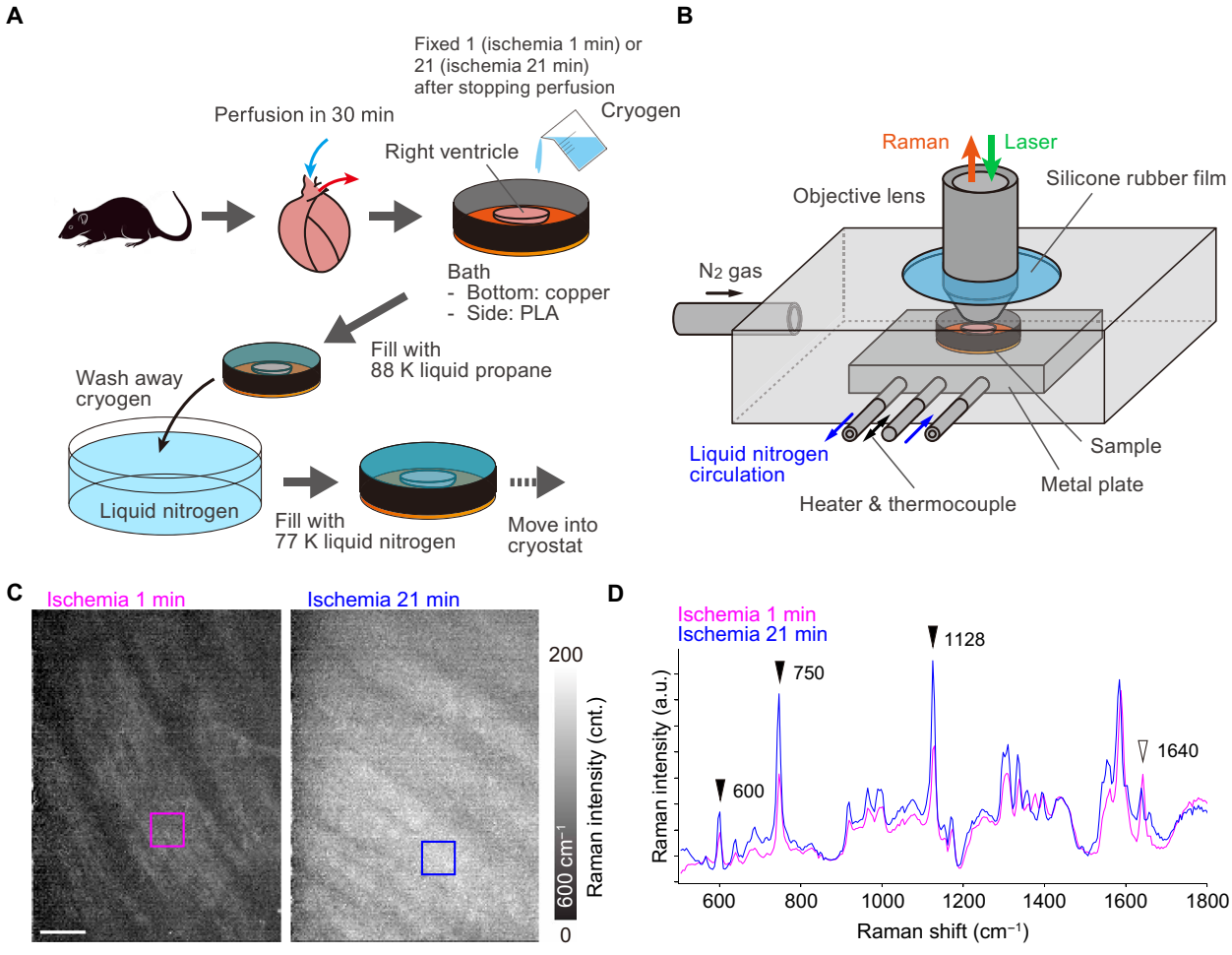

Fig. 3. Rapid freezing and low-temperature Raman imaging of a rat heart. (**A**) Procedures of the ischemic injury, rapid freezing, and subsequent transfer of the frozen myocardial tissue to the microscope cryostat (PLA, polylactic acid). (**B**) Schematic of the cryostat for tissue imaging by an upright Raman microscope. (**C**) Raman images reconstructed by the intensity at 600 cm^{-1}, assigned to reduced cytochrome c. The hearts were cryofixed at 1 min (left) and 21 min (right) after cessation of perfusion and measured at 153 K. (**D**) Raman spectra of the frozen rat hearts measured at 153 K. Magenta and blue lines exhibit average spectra taken from magenta and blue squares in (C), respectively. Scale bar, 50 μm. SVD was applied to all data to separate signals from noises (*70*).

However, the high-SNR advantage of coherent Raman microscopy can be reduced with longer exposures when autofluorescence is not prominent (*1*).

Improving the detection sensitivity in high-resolution Raman microscopy will expand the capability of optical imaging of drug substances (*52*–*54*) and bacteria (*55*), which is difficult with conventional fluorescence labeling. The high-sensitivity and high-resolution drug imaging can benefit the study of drug delivery and discovery (*56*). Label-free Raman imaging can be also applied to nondestructive analysis of cryopreserved cells and tissues before industrial and clinical uses (*57*). In vivo applications can be also realized by use of an in vivo rapid freezing technique (*58*, *59*), preserving physiological conditions of organs in living bodies and allowing interrogation by Raman microscopy. The Raman mapping of the mouse liver frozen rapidly in vivo was presented by cryopreservation of oxygenated and deoxygenated states of hemoglobin in hepatic blood vessels (*58*). In our research, the combination of the high-resolution and high-sensitivity Raman imaging technique successfully demonstrated that Raman microscopy can visualize the finer spatial variation of the hemeprotein in the tissue and its redox state at certain spatiotemporal point in living bodies while preserving physiological conditions.

In principle, SNR can be improved without limit if the exposure time can be increased without limit. In practice, however, the limit of SNR is imposed by the saturation of the charge-coupled device (CCD) element, which is typically 0.3 million to 1 million electrons/pixel. However, with multiple exposures, this limit can be easily overcome at the cost of a small amount of readout noise [a few electrons/pixel (root mean square)]. Photodamage to the sample and water crystallization (*39*) during long exposures also determine the SNR limit. Ultimately, the SNR limit is expected to depend on sample stability. The efficiency of improving the SNR with long exposures also depends on the amount and characteristics of the sample signal and background light.

In our system, the detection of signals from low-concentration molecules still competes with the background light that can originate from the substrates and optical components. For further improvement of detection sensitivity, reduction of such background light can be achieved by separating excitation and detection optical

paths (*60*) as well as by use of non-emissive sample substrates (*61*). Autofluorescence of the sample is also a concern in low-temperature Raman imaging as it tends to increase at lower sample temperatures and add noise to measured Raman spectra (fig. S9). Use of near-infrared or deep-ultraviolet wavelength excitation can help further improvement of SNR in low-temperature Raman imaging by eliminating the fluorescent background (*62*, *63*).

Another potential issue in the presented method is the formation of large ice crystals and potential sample modification. In our experiments, we did not observe formation of large ice crystals during Raman observation (fig. S3B). However, the Raman spectrum measurement indicated the formation of tiny ice crystals that cannot be observed by the spatial resolution of optical microscopy but may be found by higher-resolution imaging techniques, such as electron microscopy and super-resolution optical microscopy. Despite the initial rapid freezing process does not lead to the development of large ice crystals within cells, especially at a cooling rate of 10^4 to 10^5 K/s (*64*), elevating the temperature to evaporate the liquid propane may cause the formation of large ice crystals, depending on the cell and its intracellular state (*59*). In such a case, the liquid propane can be eliminated without increasing the temperature by rinsing with liquid nitrogen, as demonstrated in our experiments of wide-FOV imaging (Fig. 1G), multi-Raman tag imaging (Fig. 2E), and tissue measurement (Fig. 3, C and D). We observed sample thawing with a laser fluence exceeding those demonstrated above and therefore adjusted the temperature between 153 and 233 K, depending on the exposure time, while maintaining the autofluorescence low enough for Raman measurement. Keeping the sample temperature lower during Raman measurement can also avoid the ice crystal growth due to a phase transition by laser heating. Use of high-pressure freezing is effective to further suppress large ice crystal formation, especially thick samples, such as spheroids and tissues (*65*). Controlling the physical and chemical conditions surrounding the sample is key to expand the advantage of cryogenic Raman measurement further.

In our study, the temperature-dependent Raman spectral changes, such as reduced photobleaching of resonant Raman scattering, and the intramolecular structural changes were observed. It has also been reported that Raman spectrum of biological molecules can be affected by hydration and dehydration conditions (*66*), which might cause the change in Raman spectra of biological samples. This is not an issue only for low-temperature Raman imaging, but our results indicate that the sample temperature needs to be controlled to accurately interpret the measured Raman spectra.

The presented method will further attract life scientists and clinicians when combined with other modalities. The presented method is highly compatible with cryo–electron microscopy (*67*), cryogenic super-resolution fluorescence microscopy (*68*), and correlative light and electron microscopy (*69*). Such a combination allows correlative structural and chemical information for the precise analysis of biological samples, providing deep insights into biological phenomena from a chemical aspect that cannot be explored by conventional techniques.

MATERIALS AND METHODS

Cell preparation

HeLa cells were cultured on fused silica coverslips with a thickness of 0.17 ± 0.02 mm and a diameter of 25 mm (Matsunami, S339882) and maintained in Dulbecco's modified Eagle's medium (DMEM; 043-30085, Wako-Fujifilm) supplemented with 10% fetal bovine serum (FBS; S1780-500U, Biowest) and 1% penicillin-streptomycin-glutamine solution (15140122, Gibco) for 48 hours in the CO_2 incubator at 310 K (37°C). Before Raman measurements, the medium was replaced by Hanks' balanced salt solution (HBSS; 082-08961, Wako-Fujifilm).

For chemical fixation, the cells were fixed with 4% PFA (163-20145, Wako-Fujifilm) at 293 K for 20 min. The fixed cells were rinsed three times and immersed in HBSS for Raman imaging.

For EdU measurements (Fig. 2, C to E), the cells were cultured without FBS for 24 hours in a DMEM solution to synchronize cell cycle for all the cells. The medium was then replaced by a DMEM solution containing EdU at a concentration of 100 μM, and the cells were incubated for 12 hours (Fig. 2C) or 24 hours (Fig. 2E).

For AltQ2 measurements, the cells were rinsed with HBSS and incubated with AltQ2 at a concentration of 4 μM for 30 min.

For multiple Raman tag imaging, the cells were first loaded with EdU by the above-described protocol. The cells were then incubated in a DMEM solution containing MitoBADY at the concentration of 800 nM for 1 hour and subsequently loaded with AltQ2 for 30 min as mentioned above.

Tissue preparation

All of the animal experiments described in this study were conducted in accordance with the Guide for the Care and Use of Laboratory Animals (eighth edition, National Academies Press, Washington, D.C., 2011) and with approval by the Animal Research Committee at Kyoto Prefectural University of Medicine (approval no. M2022-238). Male Wistar rats at the age of 9 weeks were purchased from Shimizu Laboratory Supplies. The animals were placed under deep general anesthesia using intraperitoneal injection with medetomidine (0.1 mg/kg; Nippon Zenyaku Kogyo), midazolam (3.0 mg/kg; Sandoz), and butorphanol (5.0 mg/kg; Meiji Animal Health). After injection of heparin sodium (Mochida Pharmaceutical) into the inferior vena cava (1 U/g body weight), the hearts were quickly resected from the animals.

The excised hearts were retrogradely perfused via the aorta with oxygenated Tyrode's solution [137 mM NaCl, 4 mM KCl, 1 mM $MgCl_2$, 0.33 mM NaH_2PO_4, 1.2 mM $CaCl_2$, 10 mM Hepes, and 10 mM glucose (pH 7.4)] at 310 K with a constant pressure of 9.81 kPa for ~3 min. Then, the retrograde perfusion with oxygenated Tyrode's solution was switched to a constant flux rate of 10 ml/min, controlled by a micro tube pump (MP-3 N, Tokyo Rikakikai).

For preparation of 1-min ischemia heart, the right ventricle was cut out, placed on a copper plate, and frozen by liquid propane in 1 min after the perfusion was stopped. For preparation of 21-min ischemic heart, the whole heart was first perfused with oxygenated Tyrode's solution for more than 30 min to stabilize its redox state and subsequently perfused with Tyrode's solution with 20 mM 2,3-butanedione monoxime (10923-52, Nacalai Tesque) for 15 min to attenuate the contraction, according to the literature (*46*). Global ischemia was then induced in the heart by stopping perfusion for 20 min (*46*). Following the global ischemia, the right ventricle was cut out, placed on a copper plate, and frozen by liquid propane in 1 min.

Slit-scanning Raman microscope equipped with a cryostat

All measurements were performed by slit-scanning Raman microscopes equipped with cryostats. For cell imaging, we set a custom cryostat equipped with a cryogen introduction unit on the sample

stages of a homebuilt inverted Raman microscope system. The sample coverslip was set on the sample holder. The details of the optical setup can be seen elsewhere (*2*). Briefly, a single-frequency laser at 532-nm continuous-wave oscillation (Millennia eV, Spectra Physics or Verdi, Coherent) was used for Raman excitation. The laser intensity at the sample was set at 3.0 mW/μm^2. The laser beam was focused into a line shape by use of a cylindrical lens and focused on the sample located on an inverted microscope (Ti-E, Nikon) equipped with a 60×/0.95 numerical aperture (NA) dry objective lens (CFI Plan Apo Lambda 60XC, Nikon). The Raman scattering light generated at the sample under line illumination was collected by the same objective lens in a backscattering geometry, filtered with a longpass edge filter, and refocused at the entrance slit (60 μm, ~1.2–Airy unit confocal slit) of spectrophotometer (CLP-300 or MK-300, Bunkoukeiki) equipped with a grating of 600 grooves/mm. High–spectral resolution Raman observation (Fig. 1E; high–spectral resolution experiments in Fig. 1F and fig. S6) was performed with the slit width of entrance slit with 40 μm (~0.8–Airy unit confocal slit) and grating of 1800 grooves/mm. The one-dimensional distribution of Raman spectra at the sample irradiated by line illumination was then recorded by a cooled CCD camera (PIXIS 2048B or PIXIS 400BReXcelon, Teledyne Princeton Instruments). A galvanometer mirror was used to scan the sample to acquire a two-dimensional Raman hyperspectral image. The scanning pitch was set to 250 or 220 nm. To avoid any change in the focus position during Raman imaging, we used a focus compensation system equipped in the microscope (Nikon PFS).

For tissue imaging, we set a cryostat (THMS600, Linkam, partially customized to enable the insertion of an objective lens into the cryostat) on the sample stage of an upright slit-scanning Raman microscope commercially available (Raman-11, Nanophoton). The excitation wavelength was 532 nm, and the laser intensity at the sample was set at 1.0 mW/μm^2. The line-shaped laser beam was focused on the sample using a 20×/0.75 NA dry objective lens (UPLSAP20X, Olympus), and the Raman scattering from the sample was collected using the same objective lens with a backscattering geometry. The spectrophotometer entrance slit was set at 30 μm. The grating of 300 grooves/mm was used. The cooled CCD camera (PIXIS 400BReXcelon, Teledyne Princeton Instruments) was used to record Raman spectra. The scanning pitch was set to 1.84 μm.

The wave-number axis of Raman spectra measurement was corrected by use of ethanol Raman bands at 434, 884, 1454, and 2930 cm^{-1} as reference for cell measurements and 434, 884, 1095, and 1454 cm^{-1} as reference for tissue measurements.

Cryofixation by liquid cryogen and subsequent cooling

Liquid propane was produced by feeding gaseous propane into a beaker cooled at 77 K by liquid nitrogen. The feeding for 4 min at 0.09 MPa approximately produced 60 ml of liquid propane. The liquid propane in the beaker was at around its freezing point (~85 K) in a liquid nitrogen bath (at ~77 K) until use for cryofixation of the sample. The cryogen temperature just before use was measured with a K-type thermocouple (RS PRO) connected to a temperature controller with a function of automatic cold junction temperature compensation (KT4R, Panasonic Industrial Devices SUNX).

For the inverted microscope system, nitrogen gas was continuously introduced into the cryostat. The sample at room temperature (293 K) was frozen by introducing the liquid propane inside the cryostat. To avoid a temperature rise of liquid propane by contact with the cooling block before reaching at the sample, the cryogen introduction unit cooled with liquid nitrogen was used to guide liquid propane to the sample through the hole (with a diameter of 2 mm) of the cooling block. The cooling block was cooled by circulating liquid nitrogen inside immediately after introduction of the cryogen until reaching at a target temperature. The introduction of nitrogen gas into the cryostat was stopped by closing the vent channel of the cryostat when the temperature of cooling block became close to the target temperature. The temperature was then stabilized by a temperature feedback control on the speed of liquid nitrogen flux. The liquid propane remaining on the sample, which could interfere with Raman measurement, was removed via evaporation by either keeping the sample temperature above the propane boiling point (231 K, for Figs. 1, C to F, and 2, A to D) or introducing liquid nitrogen (for Figs. 1G and 2E and figs. S5, S8, C and D, and S9) on the sample to wash out the liquid propane. The temperature during Raman observation was chosen so that the autofluorescence, which can be increased at low temperature (fig. S9), does not strongly disturb the Raman measurement.

For the upright microscope system, the tissue sample at room temperature (293 K) located on a copper plate with a thickness of 50 μm was frozen outside the cryostat by pouring liquid propane. The copper plate having the frozen sample was immediately transferred to a liquid nitrogen bath to replace the surrounding liquid propane with liquid nitrogen. The copper plate having the frozen sample was then quickly transferred into the cryostat that was cooled down to 153 K in advance. The liquid nitrogen surrounding the sample was evaporated naturally before starting Raman measurement. The cryostat temperature was kept through the Raman imaging by liquid nitrogen circulation in the cooling block.

Data processing

Acquired Raman hyperspectral image data were analyzed using a custom software developed on MATLAB environment (R2017b, MathWorks). For all the datasets, cosmic rays were removed in each CCD frame by applying a local median filter, the bias value of CCD was subtracted, and the wave-number region of interest was cropped. Except for the quantitative signal amount and SNR improvement data shown in Fig. 2, A and B, and fig. S8, each dataset was further processed as follows: SVD was applied to a Raman hyperspectral image dataset for reconstructing it with reduced noise (*70*). Raman hyperspectral data of 5 and 40 s per line in Fig. 2C, before and after PFA fixation in Fig. 2D, were combined in each one dataset before SVD processing. Fluorescence background was subtracted from the Raman spectra with recursive polynomial fitting by the least squares method (*71*). To reconstruct Raman images, for all the datasets, a difference Raman intensity at two wave numbers was mapped. All the parameters of those data processing procedures are shown in table S2.

For the wide-field Raman image (Fig. 1G) and multi-Raman-tag imaging (Fig. 2E), unexpected horizontal stripes appeared because of defected pixels of the spectrophotometer camera. We corrected the stripes by so called striped correction process (*72*), on MATLAB environment (R2023a, MathWorks) (fig. S10). Briefly, each column of a reconstructed image was divided by the mean intensity projection of the image to the *y* axis (i.e., parallel to the line illumination) so that the stripe pattern was removed. In this process, the intensity distribution intrinsic to the sample was modified. To recover the intrinsic intensity distribution, the mean intensity projection

was smoothed by a moving average filter with 51-pixel length, and the derived smoothed signal was multiplied with the striped corrected image.

To estimate the signal amount (Fig. 2B) and SNR (fig. S8), we used the Eqs. 1 and 2 to obtain the Raman signal amount $Signal_{\nu 1}$ at a wave number ν_1 as a difference between the intensity $I_{\nu 1}$ measured at a wave number ν_1 and the peak bottom signal ($I_{\nu 2}$) at a wave number ν_2 that corresponds to the background at wave number ν_1 to be detected without Raman signal. Because the total noise amount given by the photon shot noise, dark count, and readout noise exhibits Poisson distribution, the noise at the wave number ν_1 is estimated as the square root of $I_{\nu 1}$ as shown equation Eq. 2. We chose (745, 732), (2848, 2781), and (2934, 2842) cm^{-1} as (ν_1, ν_2) for cytochromes, lipid, and protein, respectively. $I_{\nu 1}$ and $I_{\nu 2}$ were obtained as mean values of 12 random areas, which showed relatively strong Raman signals at the wave number of interest in Fig. 2A (5 × 5 pixels for cytochromes and lipid and 10 × 10 pixels for protein) by using ImageJ (1.54f). The plot of each band in Fig. 2B was fitted to a linear function using the least squares method with a home-made Python program, as the Raman signal is expected to increase linearly with exposure time.

$$Signal_{\nu 1} = I_{\nu 1} - I_{\nu 2} \quad (1)$$

$$SNR_{\nu 1} = \frac{I_{\nu 1} - I_{\nu 2}}{\sqrt{I_{\nu 1}}} \quad (2)$$

Calculation of local heating during low-temperature Raman measurement

To calculate local heating by laser irradiation, we made a sample model containing FAD and cytochrome c as main light absorbers at the used wavelength for temperature calculation by COMSOL (version 6.2, COMSOL Inc.) in fig. S2E. Absorber was put in an ice layer on a substrate. Cooling block that has a 2-mm-diameter hole was put on the ice layer. In this model, temperature of a boundary between ice layer and cooling block was kept in 233 K. This model was insulated at other boundaries. Absorbance of FAD and reduced cytochrome c were estimated by calculating molar extinction coefficient and estimating intracellular concentration of FAD and reduced cytochrome c. The molar extinction coefficient was calculated from the excitation spectrum obtained by measuring solutions of FAD and reduced cytochrome c with known concentrations by a spectrophotometer, and the intracellular concentration of each molecule was estimated from the fluorescence and Raman signal intensity of the cell using a calibration curve obtained by measuring a solution with known concentration. The parameters used in the calculation such as size, absorbance, thermal conductivity, heat capacity, and density were listed in table S1. In the calculation, line-shaped illumination region was assumed with a rectangle having uniform intensity distribution (3.0 $mW/\mu m^2$), an irradiation time of 70 s, and a wavelength of 532 nm. The light passed through a planar region in a range (0.6 μm by 200 μm) from bottom to top.

Supplementary Materials

This PDF file includes:

Figs. S1 to S10
Tables S1 and S2
References

REFERENCES AND NOTES

1. J.-X. Cheng, W. Min, Y. Ozeki, D. Polli, *Stimulated Raman Scattering Microscopy: Techniques and Applications* (Elsevier, 2021).
2. Y. Kumamoto, M. Li, K. Koike, K. Fujita, Slit-scanning Raman microscopy: Instrumentation and applications for molecular imaging of cell and tissue. *J. Appl. Phys.* **132**, 171101 (2022).
3. B. G. Saar, C. W. Freudiger, J. Reichman, C. M. Stanley, G. R. Holtom, X. S. Xie, Video-rate molecular imaging in vivo with stimulated Raman scattering. *Science* **330**, 1368–1370 (2010).
4. M. Li, Y. Nawa, S. Ishida, Y. Kanda, S. Fujita, K. Fujita, Label-free chemical imaging of cytochrome P450 activity by Raman microscopy. *Commun. Biol.* **5**, 778 (2022).
5. K. Aljakouch, T. Lechtonen, H. K. Yosef, M. K. Hammoud, W. Alsaidi, C. Kötting, C. Mügge, R. Kourist, S. F. El-Mashtoly, K. Gerwert, Raman microspectroscopic evidence for the metabolism of a tyrosine kinase inhibitor, neratinib, in cancer cells. *Angew. Chem. Int. Ed. Engl.* **57**, 7250–7254 (2018).
6. Z. Farhane, F. Bonnier, A. Casey, H. J. Byrne, Raman micro spectroscopy for in vitro drug screening: Subcellular localisation and interactions of doxorubicin. *Analyst* **140**, 4212–4223 (2015).
7. E. Brauchle, A. Knopf, H. Bauer, N. Shen, S. Linder, M. G. Monaghan, K. Ellwanger, S. L. Layland, S. Y. Brucker, A. Nsair, K. Schenke-Layland, Non-invasive chamber-specific identification of cardiomyocytes in differentiating pluripotent stem cells. *Stem Cell Reports* **6**, 188–199 (2016).
8. G. Pettinato, M. F. Coughlan, X. Zhang, L. Chen, U. Khan, M. Glyavina, C. J. Sheil, P. K. Upputuri, Y. N. Zakharov, E. Vitkin, A. B. D'Assoro, R. A. Fisher, I. Itzkan, L. Zhang, L. Qiu, L. T. Perelman, Spectroscopic label-free microscopy of changes in live cell chromatin and biochemical composition in transplantable organoids. *Sci. Adv.* **7**, eabj2800 (2021).
9. K. Kong, C. Kendall, N. Stone, I. Notingher, Raman spectroscopy for medical diagnostics - From in-vitro biofluid assays to in-vivo cancer detection. *Adv. Drug Deliv. Rev.* **89**, 121–134 (2015).
10. Z. Liu, W. Su, J. Ao, M. Wang, Q. Jiang, J. He, H. Gao, S. Lei, J. Nie, X. Yan, X. Guo, P. Zhou, H. Hu, M. Ji, Instant diagnosis of gastroscopic biopsy via deep-learned single-shot femtosecond stimulated Raman histology. *Nat. Commun.* **13**, 4050 (2022).
11. J. N. Taylor, K. Mochizuki, K. Hashimoto, Y. Kumamoto, Y. Harada, K. Fujita, T. Komatsuzaki, High-resolution raman microscopic detection of follicular thyroid cancer cells with unsupervised machine learning. *J. Phys. Chem. B* **123**, 4358–4372 (2019).
12. A. Downes, A. Elfick, Raman spectroscopy and related techniques in biomedicine. *Sensors* **10**, 1871–1889 (2010).
13. Y. Tan, S. O. Konorov, H. G. Schulze, J. M. Piret, M. W. Blades, R. F. B. Turner, Comparative study using Raman microspectroscopy reveals spectral signatures of human induced pluripotent cells more closely resemble those from human embryonic stem cells than those from differentiated cells. *Analyst* **137**, 4509–4515 (2012).
14. H. Yamakoshi, K. Dodo, A. Palonpon, J. Ando, K. Fujita, S. Kawata, M. Sodeoka, Alkyne-tag Raman imaging for visualization of mobile small molecules in live cells. *J. Am. Chem. Soc.* **134**, 20681–20689 (2012).
15. Y. Shen, F. Hu, W. Min, Raman imaging of small biomolecules. *Annu. Rev. Biophys.* **48**, 347–369 (2019).
16. L. Wei, Z. Chen, L. Shi, R. Long, A. V. Anzalone, L. Zhang, F. Hu, R. Yuste, V. W. Cornish, W. Min, Super-multiplex vibrational imaging. *Nature* **544**, 465–470 (2017).
17. F. Hu, C. Zeng, R. Long, Y. Miao, L. Wei, Q. Xu, W. Min, Supermultiplexed optical imaging and barcoding with engineered polyynes. *Nat. Methods* **15**, 194–200 (2018).
18. V. V. Pully, A. T. M. Lenferink, C. Otto, Time-lapse Raman imaging of single live lymphocytes. *J. Raman Spectrosc.* **42**, 167–173 (2011).
19. C. K. Huang, M. Ando, H. O. Hamaguchi, S. Shigeto, Disentangling dynamic changes of multiple cellular components during the yeast cell cycle by in vivo multivariate Raman imaging. *Anal. Chem.* **84**, 5661–5668 (2012).
20. M. Okada, N. I. Smith, A. F. Palonpon, H. Endo, S. Kawata, M. Sodeoka, K. Fujita, Label-free Raman observation of cytochrome c dynamics during apoptosis. *Proc. Natl. Acad. Sci. U.S.A.* **109**, 28–32 (2012).
21. A. J. Hobro, N. I. Smith, An evaluation of fixation methods: Spatial and compositional cellular changes observed by Raman imaging. *Vib. Spectrosc.* **91**, 31–45 (2017).
22. T. Ichikawa, D. Wang, K. Miyazawa, K. Miyata, M. Oshima, T. Fukuma, Chemical fixation creates nanoscale clusters on the cell surface by aggregating membrane proteins. *Commun. Biol.* **5**, 487 (2022).
23. M. M. Mariani, P. Lampen, J. Popp, B. R. Wood, V. Deckert, Impact of fixation on in vitro cell culture lines monitored with Raman spectroscopy. *Analyst* **134**, 1154–1161 (2009).
24. J. Huebinger, J. Spindler, K. J. Holl, B. Koos, Quantification of protein mobility and associated reshuffling of cytoplasm during chemical fixation. *Sci. Rep.* **8**, 17756 (2018).
25. L. Maneta-Peyret, P. Compère, P. Moreau, G. Goffinet, C. Cassagne, Immunocytochemistry of lipids: Chemical fixatives have dramatic effects on the preservation of tissue lipids. *Histochem. J.* **31**, 541–547 (1999).

26. P. R. Carey, J. Dong, Following ligand binding and ligand reactions in proteins via Raman crystallography. *Biochemistry* **43**, 8885–8893 (2004).
27. K. A. Okotrub, N. V. Surovtsev, Raman scattering evidence of hydrohalite formation on frozen yeast cells. *Cryobiology* **66**, 47–51 (2013).
28. T. K. Tsang, E. A. Bushong, D. Boassa, J. Hu, B. Romoli, S. Phan, D. Dulcis, C. Y. Su, M. H. Ellisman, High-quality ultrastructural preservation using cryofixation for 3D electron microscopy of genetically labeled tissues. *eLife* **7**, e35524 (2018).
29. M. H. Laporte, N. Klena, V. Hamel, P. Guichard, Visualizing the native cellular organization by coupling cryofixation with expansion microscopy (Cryo-ExM). *Nat. Methods* **19**, 216–222 (2022).
30. J. Huebinger, H. Grecco, M. E. Masip, J. Christmann, G. R. Fuhr, P. I. H. Bastiaens, Ultrarapid cryo-arrest of living cells on a microscope enables multiscale imaging of out-of-equilibrium molecular patterns. *Sci. Adv.* **7**, eabk0882 (2021).
31. T. Sugimura, S. Kajimoto, T. Nakabayashi, Label-free imaging of intracellular temperature by using the O–H stretching raman band of water. *Angew. Chem. Int. Ed. Engl.* **59**, 7755–7760 (2020).
32. K. A. Okotrub, V. I. Mokrousova, S. Y. Amstislavsky, N. V. Surovtsev, Lipid droplet phase transition in freezing cat embryos and oocytes probed by Raman spectroscopy. *Biophys. J.* **15**, 577–587 (2018).
33. H. Okamoto, Y. Sekimoto, M. Tasumi, Assignment and anharmonicity analysis of overtone and combination bands observed in the resonance Raman spectra of carotenoids. *Spectrochim. Acta A Mol. Spectrosc.* **50**, 1467–1473 (1994).
34. M. A. Welte, A. P. Gould, Lipid droplet functions beyond energy storage. *Biochim. Biophys. Acta Mol. Cell Biol. Lipids* **1862**, 1260–1272 (2017).
35. K. A. Okotrub, N. V. Surovtsev, Redox state of cytochromes in frozen yeast cells probed by resonance raman spectroscopy. *Biophys. J.* **109**, 2227–2234 (2015).
36. M. Kakita, M. Okuno, H. O. Hamaguchi, Quantitative analysis of the redox states of cytochromes in a living L929 (NCTC) cell by resonance Raman microspectroscopy. *J. Biophotonics* **6**, 256–259 (2013).
37. M. F. Nonier, N. V. De Gaulejac, N. Vivas, C. Vitry, Characterization of carotenoids and their degradation products in oak wood. Incidence on the flavour of wood. *C. R. Chim.* **7**, 689–698 (2004).
38. S. Limbo, L. Torri, L. Piergiovanni, Light-induced changes in an aqueous β-carotene system stored under halogen and fluorescent lamps, affected by two oxygen partial pressures. *J. Agric. Food Chem.* **55**, 5238–5245 (2007).
39. J. C. Gilkey, L. A. Staehelin, Advances in ultrarapid freezing for the preservation of cellular ultrastructure. *J. Electron Microsc. Tech.* **3**, 177–210 (1986).
40. J. Ma, X. Yang, Y. Sun, J. Yang, Thermal damage in three-dimensional vivo bio-tissues induced by moving heat sources in laser therapy. *Sci. Rep.* **9**, 10987 (2019).
41. S. Matsui, Y. Tsujimoto, K. Matsushima, Stimulatory effects of hydroxyl radical generation by Ga-Al-As laser irradiation on mineralization ability of human dental pulp cells. *Biol. Pharm. Bull.* **30**, 27–31 (2007).
42. K. A. K. Tanaka, K. G. N. Suzuki, Y. M. Shirai, S. T. Shibutani, M. S. H. Miyahara, H. Tsuboi, M. Yahara, A. Yoshimura, S. Mayor, T. K. Fujiwara, A. Kusumi, Membrane molecules mobile even after chemical fixation. *Nat. Methods* **7**, 865–866 (2010).
43. P. Tang, W. Cheng, X. He, Q. Zhang, J. Zhong, X. Lu, S. Liu, L. Zhong, Raman spectrum spectral imaging revealing the molecular mechanism of Berberine-induced Jurkat cell apoptosis and the receptor-mediated Berberine delivery system. *Biomed. Opt. Express* **10**, 1581–1600 (2019).
44. H. Yamakoshi, A. Palonpon, K. Dodo, J. Ando, S. Kawata, K. Fujita, M. Sodeoka, A sensitive and specific Raman probe based on bisarylbutadiyne for live cell imaging of mitochondria. *Bioorg. Med. Chem. Lett.* **25**, 664–667 (2015).
45. J. Dong, J. Malsam, J. C. Bischof, A. Hubel, A. Aksan, Spatial distribution of the state of water in frozen mammalian cells. *Biophys. J.* **99**, 2453–2459 (2010).
46. H. Fujioka, M. Kawatani, S. J. Spratt, A. Komazawa, Y. Misawa, J. Shou, T. Mizuguchi, H. Kosakamoto, R. Kojima, Y. Urano, F. Obata, Y. Ozeki, M. Kamiya, Activatable Raman probes utilizing enzyme-induced aggregate formation for selective ex vivo imaging. *J. Am. Chem. Soc.* **145**, 8871–8881 (2023).
47. S. Ohira, H. Tanaka, Y. Harada, T. Minamikawa, Y. Kumamoto, S. Matoba, H. Yaku, T. Takamatsu, Label-free detection of myocardial ischemia in the perfused rat heart by spontaneous Raman spectroscopy. *Sci. Rep.* **7**, 42401 (2017).
48. N. A. Brazhe, M. Treiman, A. R. Brazhe, N. L. Find, G. V. Maksimov, O. V. Sosnovtseva, Mapping of redox state of mitochondrial cytochromes in live cardiomyocytes using Raman microspectroscopy. *PLOS ONE* **7**, e41990 (2012).
49. K. Ikemoto, K. Hashimoto, Y. Harada, Y. Kumamoto, M. Hayakawa, K. Mochizuki, K. Matsuo, K. Yashiro, H. Yaku, T. Takamatsu, H. Tanaka, Raman spectroscopic assessment of myocardial viability in langendorff-perfused ischemic rat hearts. *Acta Histochem. Cytochem.* **54**, 65–72 (2021).
50. K. A. Okotrub, N. V. Surovtsev, Effect of glycerol on photobleaching of cytochrome Raman lines in frozen yeast cells. *Eur. Biophys. J.* **47**, 655–662 (2018).
51. C. Kallepitis, M. S. Bergholt, M. M. Mazo, V. Leonardo, S. C. Skaalure, S. A. Maynard, M. M. Stevens, Quantitative volumetric Raman imaging of three dimensional cell cultures. *Nat. Commun.* **8**, 14843 (2017).
52. Y. Harada, P. Dai, Y. Yamaoka, M. Ogawa, H. Tanaka, K. Nosaka, K. Akaji, T. Takamatsu, Intracellular dynamics of topoisomerase I inhibitor, CPT-11, by slit-scanning confocal Raman microscopy. *Histochem. Cell Biol.* **132**, 39–46 (2009).
53. S. F. El-Mashtoly, D. Petersen, H. K. Yosef, A. Mosig, A. Reinacher-Schick, C. Kötting, K. Gerwert, Label-free imaging of drug distribution and metabolism in colon cancer cells by Raman microscopy. *Analyst* **139**, 1155–1161 (2014).
54. K. Koike, K. Bando, J. Ando, H. Yamakoshi, N. Terayama, K. Dodo, N. I. Smith, M. Sodeoka, K. Fujita, Quantitative drug dynamics visualized by alkyne-tagged plasmonic-enhanced Raman microscopy. *ACS Nano* **14**, 15032–15041 (2020).
55. L. Cui, K. Yang, H.-Z. Li, H. Zhang, J.-Q. Su, M. Paraskevaidi, F. L. Martin, B. Ren, Y.-G. Zhu, Functional single-cell approach to probing nitrogen-fixing bacteria in soil communities by resonance Raman spectroscopy with $^{15}N_2$ labeling. *Anal. Chem.* **90**, 5082–5089 (2018).
56. S. Vanden-Hehir, W. J. Tipping, M. Lee, V. G. Brunton, A. Williams, A. N. Hulme, Raman imaging of nanocarriers for drug delivery. *Nanomaterials* **9**, 341 (2019).
57. R. Li, K. Hornberger, J. R. Dutton, A. Hubel, Cryopreservation of human iPS cell aggregates in a DMSO-free solution—An optimization and comparative study. *Front. Bioeng. Biotechno.* **8**, 1 (2020).
58. N. Ohno, N. Terada, S. Ohno, Histochemical analyses of living mouse liver under different hemodynamic conditions by "in vivo cryotechnique". *Histochem. Cell Biol.* **126**, 389–398 (2006).
59. N. Terada, N. Ohno, S. Saitoh, S. Ohno, Application of 'in vivo cryotechnique' to detect erythrocyte oxygen saturation in frozen mouse tissues with confocal Raman cryomicroscopy. *J. Struct. Biol.* **163**, 147–154 (2008).
60. K. Bando, S. Yabuuchi, M. Li, T. Kubo, R. Oketani, N. I. Smith, K. Fujita, Bessel-beam illumination Raman microscopy. *Biomed. Opt. Express* **13**, 3161–3170 (2022).
61. A. T. Lewis, R. Gaifulina, M. Isabelle, J. Dorney, M. L. Woods, G. R. Lloyd, K. Lau, M. Rodriguez-Justo, C. Kendall, N. Stone, G. M. Thomas, Mirrored stainless steel substrate provides improved signal for Raman spectroscopy of tissue and cells. *J. Raman Spectrosc.* **48**, 119–125 (2017).
62. M.-J. Anita, R.-K. Rebecca, Raman spectroscopy for the detection of cancers and precancers. *J. Biomed. Opt.* **1**, 31–70 (1995).
63. S. Chadha, W. H. Nelson, J. F. Sperry, Ultraviolet micro-Raman spectrograph for the detection of small numbers of bacterial cells. *Rev. Sci. Instrum.* **64**, 3088–3093 (1993).
64. H. Bank, Visualization of freezing damage. II. Structural alterations during warming. *Cryobiology* **10**, 157–170 (1973).
65. P. Monaghan, N. Perusinghe, M. Müller, High-pressure freezing for immunocytochemistry. *J. Microsc.* **192**, 248–258 (1998).
66. V. Kocherbitov, J. Latynis, A. Misiuì, J. Barauskas, G. Niaura, Hydration of lysozyme studied by Raman spectroscopy. *J. Phys. Chem. B* **117**, 4981–4992 (2013).
67. P. Schultz, Cryo-electron microscopy of vitrified specimens. *Q. Rev. Biophys.* **21**, 129–228 (1988).
68. R. Kaufmann, P. Schellenberger, E. Seiradake, I. M. Dobbie, E. Y. Jones, I. Davis, C. Hagen, K. Grünewald, Super-resolution microscopy using standard fluorescent proteins in intact cells under cryo-conditions. *Nano Lett.* **14**, 4171–4175 (2014).
69. D. P. Hoffman, G. Shtengel, C. S. Xu, K. R. Campbell, M. Freeman, L. Wang, D. E. Milkie, H. A. Pasolli, N. Iyer, J. A. Bogovic, D. R. Stabley, A. Shirinifard, S. Pang, D. Peale, K. Schaefer, W. Pomp, C.-L. Chang, J. Lippincott-Schwartz, T. Kirchhausen, D. J. Solecki, E. Betzig, H. F. Hess, Correlative three-dimensional super-resolution and block-face electron microscopy of whole vitreously frozen cells. *Science* **367**, eaaz5357 (2020).
70. H.-J. V. Manen, Y. M. Kraan, D. Roos, C. Otto, Intracellular chemical imaging of heme-containing enzymes involved in innate immunity using resonance Raman microscopy. *J. Phys. Chem. B* **108**, 18762–18771 (2004).
71. C. A. Lieber, A. Mahadevan-Jansen, Automated method for subtraction of fluorescence from biological raman spectra. *Appl. Spectrosc.* **57**, 1363–1367 (2003).
72. K. Mochizuki, Y. Kumamoto, S. Maeda, M. Tanuma, A. Kasai, M. Takemura, Y. Harada, H. Hashimoto, H. Tanaka, N. I. Smith, K. Fujita, High-throughput line-illumination Raman microscopy with multislit detection. *Biomed. Opt. Express* **14**, 1015–1026 (2023).
73. R. M. Pope, E. S. Fry, Absorption spectrum (380–700 nm) of pure water. II. Integrating cavity measurements. *Appl. Opt.* **36**, 8710–8723 (1997).
74. O. Haida, T. Matsuo, H. Suga, S. Seki, Calorimetric study of the glassy state X. Enthalpy relaxation at the glass-transition temperature of hexagonal ice. *J. Chem. Thermodynamics* **6**, 815–825 (1974).
75. G. A. Slack, Thermal conductivity of ice. *Phys. Rev. B.* **22**, 3065–3071 (1980).
76. K.-H. Liu, Y. Zhang, J.-J. Lee, C.-C. Chen, Y.-Q. Yeh, S.-H. Chen, C.-Y. Mou, Density and anomalous thermal expansion of deeply cooled water confined in mesoporous silica investigated by synchrotron X-ray diffraction. *J. Chem. Phys.* **139**, 064502 (2013).

Acknowledgments: We thank to S. Kawano for development of the Raman spectral imaging software; Q. Li and T. Nagano, former members of Department of Applied Physics at Osaka University, and M. Hayakawa for helping conduction of experiments; and K. Tsuji and J. Liang for useful suggestions for the experiments. **Funding:** This work was supported by JST CREST grant JPMJCR1925 (K.F.), JST COI-NEXT grant JPMJPF2009 (K.F.), and JST SPRING grant

JPMJSP2138 (K.Mi.). **Author contributions:** Project administration: K.F. Conceptualization: K.Mi., Y.K., Y.H., N.I.S., M.S., and K.F. Supervision: N.I.S., M.S., and K F. Methodology: K.Mi., Y.K., S.T., M.Y., K.Mo., Y.H., N.I.S., and K.F. Investigation: K.Mi., Y.K., S.T., K.Mo., M.L., and Y.H. Resources: Y.K., K.Mo., S.E., K.D., Y.H., M.S., and H.T. Validation: K.Mi., Y.K., S.T., M.L., Y.H., N.I.S., H.T., and K.F. Data curation: K.Mi. Formal analysis: K.Mi. Software: K.Mi. Visualization: K.Mi., Y.K., Y.H., and K.F. Writing—original draft: K.Mi., Y.K., S.T., and K F. Writing—review and editing: K.Mi., S.E., K.D., Y.H., N.I.S., and M.S. Funding acquisition: K.Mi., M.S., H.T., and K.F. **Competing interests:** K.F. and Y.K. are inventors on the patent related to this work (application number: PCT/JP2022/020045, applicant: Osaka University, publication date: 17 November 2022, publication number: WO 2022/239830 A1), and then PCT national phase applications have been filed in the United States, Japan, Europe, and China. K.F., M.Y., and Y.K. have patent applications (application number: PCT/JP2023/038854, applicant: Osaka University). K.F. is a cofounder and the chief technology officer (CTO) of Millde Co. Ltd. The authors declare that they have no additional conflict of interest. **Data and materials availability:** All data needed to evaluate the conclusions in the paper are present in the paper and/or the Supplementary Materials.

Submitted 17 November 2023
Accepted 16 May 2024
Published 11 December 2024
10.1126/sciadv.adn0110